THESIS FOR THE DEGREE OF LICENTIATE OF ENGINEERING

Modeling Ion Diffusion in Mixed-Halide Perovskites

Priyanka Deswal

Department of Physics and Astronomy
CHALMERS UNIVERSITY OF TECHNOLOGY
Göteborg, Sweden 2026

Modeling Ion Diffusion in Mixed-Halide Perovskites
Priyanka Deswal

Department of Physics and Astronomy
Chalmers University of Technology
se-412 96 Göteborg, Sweden

Cover: Defect-mediated ion migration pathways in mixed-halide perovskites.

Chalmers digitaltryck
Göteborg, Sweden 2026

Modeling Ion Diffusion in Mixed-Halide Perovskites

Priyanka Deswal
Department of Physics and Astronomy
Chalmers University of Technology

Abstract

Halide perovskites have attracted significant attention for optoelectronic applications due to their high efficiency and tunable optoelectronic properties. However, their long-term stability remains limited, largely due to the soft and polarizable lattice, which facilitates defect formation and ion migration. Understanding defect-mediated ion transport is therefore essential for improving material stability. In this thesis, ion transport in inorganic halide perovskites is investigated across multiple length scales. At the atomic level, density functional theory (DFT) combined with the nudged elastic band (NEB) method is used to study defect-mediated ion migration in $CsPbX_3$ (X = I, Br, Cl). The results demonstrate that migration barriers depend not only on intrinsic material properties but also on computational methodology, including migration pathways, exchange–correlation functionals, defect charge state, and spin–orbit coupling. Structural factors such as lattice relaxation, volume, and the local bonding environment are found to play a central role. At larger length and time scales, ion diffusion in mixed compositions $Cs_{1-x}Rb_xPbBr_{3(1-y)}I_{3y}$ is investigated using molecular dynamics simulations based on neuroevolution-based machine-learned interatomic potential. Diffusion coefficients are evaluated across a range of temperatures and compositions and analyzed using Arrhenius behavior, enabling direct comparison of activation energies and prefactors. The results show that ion transport is governed by both energetic and dynamical factors and is strongly influenced by composition and lattice flexibility, linking atomistic migration mechanisms to macroscopic diffusion behavior.

Keywords: Mixed-halide perovskites, ion diffusion, defects, nudged elastic band, machine learning, Neuroevolution potentials, activation energy, ionic transport.

LIST OF APPENDED PAPERS

This thesis consists of an introductory text and the following papers:

I **Benchmarking Halide Migration Barriers in $CsPbX_3$: Sensitivity to DFT Choices**
Priyanka Deswal, Paul Erhart, Julia Wiktor
Submitted to Physical Review Materials

II **Vacancy migration in mixed halide perovskites**
Priyanka Deswal, Erik Fransson, Benjamin M. Gallant, Dominik J. Kubicki, Julia Wiktor, Paul Erhart
In manuscript

III **Atomic-level dynamics of ion migration in metal halide perovskites**
Benjamin M. Gallant, **Priyanka Deswal**, Shrestha Banerjee, Erik Fransson, Jem Hammerton, Michael Walters, William Burston, Paul Erhart, Julia Wiktor, Dominik J. Kubicki
In manuscript

The author's contribution to the papers:

I The author performed calculations, analysis, prepared figures, and wrote the manuscript.

II The author performed calculations using a trained model, carried out the analysis, and wrote parts of the manuscript.

III The author performed simulations, conducted computational analysis, contributed to writing the computational sections.

Contents

1

Introduction

In recent years, the transition toward sustainable energy technologies has driven significant interest in new classes of functional materials. Halide perovskites (HPs) have emerged as promising materials for device applications due to their rapid performance growth and low-cost processing. Their power conversion efficiency has increased from 4% in 2009 [1] to over 27% in 2026 [2]. The success of HPs arises from their excellent optoelectronic properties, including strong optical absorption, long carrier diffusion lengths, and tunable bandgaps [3, 4]. These properties can be tuned through compositional engineering of their ABX_3-type crystal structure [3, 5], where A- and B-site cations and the X-site halides can be substituted. For example, mixing cations such as Cs and Rb or halides such as I, Br, or Cl enables systematic tuning of structural and electronic properties.

This compositional flexibility originates from their soft and polarizable lattice [6]. In HPs, the lattice is soft, because it exhibits low-frequency vibrational modes and large atomic displacements due to weak bonding and high polarizability [7, 8]. However, this same lattice softness also leads to intrinsic instability due to ion motion [9, 10]. The thermodynamics stablity of material is governed by relative free energies of competing phases, ion migration provides the means for the system to evolve toward these more stable configurations. Low migration barriers facilitate ion motion within the crystal lattice, which enable the structural rearrangements linked to degradation phenomena such as phase segregation, phase transformation, current–voltage hysteresis, and long-term performance loss [11, 12]. Therefore, improving stability requires a fundamental understanding of ion motion [13]. At the microscopic level, ion migration occurs via thermally activated hopping between lattice sites and is mediated by intrinsic point defects such as vacancies and interstitials [14, 15]. These defects are present due to thermodynamic conditions during crystal growth and provide pathways for ionic transport [13, 16]. Halide vacancies are generally the dominant defect type due to their low

formation energies, while interstitials become relevant under halide-rich conditions [17, 18]. The migration process is governed by activation barriers that depend on the local atomic environment and composition [17, 18]. At the atomic scale, first-principles calculations based on density functional theory (DFT) using the Nudged elastic band (NEB) method are commonly used to determine ion migration pathways and activation energies [19]. However, in the case of HPs the reported migration barriers show significant variation, possibly due to differences in computational methodology such as the exchange–correlation functional, charge state, or inclusion of relativistic effects [15, 20]. This motivates systematic benchmarking of defect-mediated ion migration with respect to methodological choices, including exchange–correlation functionals, charge states, migration pathways, and spin–orbit coupling, thereby enabling a consistent comparison.

Beyond pure compounds, compositional engineering provides a way to control ion migration. Substitution of cations and halides modifies lattice dimensions, local structure, and bonding characteristics, which in turn influence ionic transport [21, 22]. Studying these effects requires methods that can describe both compositional disorder and finite-temperature dynamics. While DFT provides detailed atomistic insight, it is computationally expensive for large systems and long time scales. To address this limitation, we use a machine learned interatomic potential (MLIP) based on Neuro-evolution potential (NEP) trained on DFT data, including structures of defects and migration pathways [13, 15, 18]. These models enable MD simulations to calculate ion diffusion in larger supercells and at finite temperatures, allowing us to connect atomistic migration mechanisms with macroscopic diffusion behavior.

This thesis aims to provide a consistent framework for understanding ion migration in HPs by combining DFT benchmarking with machine learning (ML) approaches, bridging atomistic mechanisms and macroscopic transport across different compositions and length scales.

1.1 Thesis overview

The work in this thesis is motivated by the following research questions:

- How sensitive is the halide migration barrier to DFT choices?
- How do A-site and halide mixing affect halide ion diffusion in $Cs_{1-x}Rb_xPbBr_{3(1-y)}I_{3y}$, and which term in the Arrhenius relation primarily controls the diffusion process?

To address these questions, Chapter 2 provides an overview of HPs, their structural stability, and the role of point defects. Chapter 3 then discusses defect-mediated ion migration at the atomistic level, including migration mechanisms, the factors affecting mi-

gration, and the sensitivity of migration barriers to computational choices. This forms the basis for the benchmarking study presented in Paper I, which addresses the first question. Chapter 4 focuses on ion diffusion in mixed $Cs_{1-x}Rb_xPbBr_{3(1-y)}I_{3y}$, where MD simulations based on MLIPs are used to extract mean squared displacements and diffusion coefficients, which are then analyzed using the Arrhenius relation. This enables the analysis presented in Paper II, addressing the second question. Finally, the comparison of computational results with experimental observations provides the basis for Paper III, carried out in collaboration with experimentalists. Together, these studies provide a consistent framework for understanding ion migration and diffusion in HPs across different length and time scales.

2

Halide perovskites

This chapter introduces HPs with emphasis on their crystal structure, stability, and defect properties. The aim is to provide the background needed to understand instability, defect formation, and ion migration in these materials.

2.1 Introduction to perovskites

Perovskite materials have the general ABX_3 formula, where a monovalent A-cation occupies the cuboctahedral cavities of a corner-sharing BX_6 octahedral framework formed by divalent B-cations and monovalent X-anions (X = Cl, Br, I) [23, 24]. The structure of $CsPbX_3$ is illustrated in Figure 2.1. The first perovskite mineral, $CaTiO_3$, was discovered in 1839. Inorganic cesium lead halides ($CsPbX_3$) were later synthesized in 1893, and their perovskite structure was confirmed in 1958, [23] with early studies focusing mainly on structural properties. The application of HPs in photovoltaics was demonstrated by Kojima *et al.* in 2009, reporting $CH_3NH_3PbI_3$ solar cells with an efficiency of 3.8% [1]. This was followed by the first all-inorganic $CsPbI_3$ solar cell, which was demonstrated in 2016 with 2.9% efficiency [25]. Wang *et al.* later improved this to 15.07% with enhanced thermal stability compared to hybrid counterparts [26]. Since then, the efficiency of HP solar cells has increased to over 27% [2].

The performance of $CsPbX_3$ perovskites is attributed to their optoelectronic properties, including strong optical absorption, long carrier diffusion length, defect tolerance, and tunable band gaps [27–29]. Their compositional flexibility allows systematic tuning of these properties through substitution at A- or X-sites [5, 29, 30]. In addition, solution-based processing enables low-cost and scalable fabrication. However, HPs exhibit limited stability under operating conditions [31]. In contrast to silicon-based devices, which can operate for decades, perovskite devices degrade on much shorter

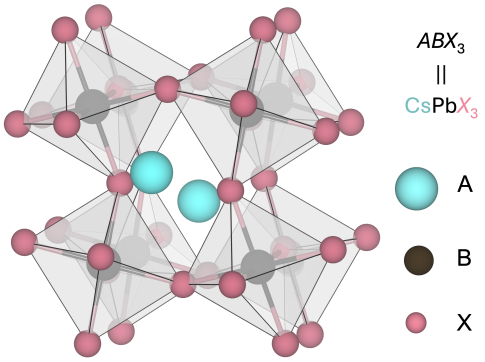

Figure 2.1: Schematic representation of the $CsPbX_3$ perovskite structure, showing the corner-sharing PbX_6 octahedral framework and the positions of the A-site (Cs^+), B-site (Pb^{2+}), and X-site (X^- = I^-, Br^-, Cl^-) anions.

timescales [11, 32]. Understanding the origin of this instability is therefore essential for their practical use. Furthermore, the presence of toxic lead raises environmental concerns. Despite this, lead-based HPs remain the most extensively studied systems due to their superior optoelectronic performance and high efficiencies, which motivates efforts toward improved encapsulation and the development of lead-free alternatives.

2.2 The issue of instability in lead HPs

Instability in lead HPs arises from both external conditions and intrinsic material properties [6, 31]. Exposure to moisture, oxygen, illumination, and elevated temperature can lead to degradation through phase decomposition or chemical change [33–37]. Although encapsulation and passivation strategies can mitigate these effects, maintaining stability under operating conditions remains challenging [28, 38]. In addition to these external factors, the bonding and structural characteristics of HPs contribute to their intrinsic instability [39, 40]. Compared to conventional covalent semiconductors, these materials exhibit mixed ionic–covalent bonding with relatively weak and anharmonic interactions, resulting in a soft and polarizable lattice [6, 14]. This allows the structure to accommodate distortions at relatively low energetic cost [7]. As a result, deviations from the ideal cubic symmetry are common, typically in the form of octahedral tilting and symmetry lowering [41, 42]. The tendency toward such distortions is described using the Goldschmidt tolerance factor,

$$t = \frac{r_A + r_X}{\sqrt{2}(r_B + r_X)}, \tag{2.1}$$

where r_A, r_B, and r_X are the ionic radii of the A-site cation, B-site cation, and halide ion, respectively. Values of t close to unity indicate cubic structures with untitled octahedra, while deviations from unity induce lower-symmetry phases with octahedral tilting that enable low-energy pathways for ion migration [39, 43, 44]. These structural features also influence defect formation and lattice dynamics, which are discussed in the following section.

2.3 Defects in halide perovskites

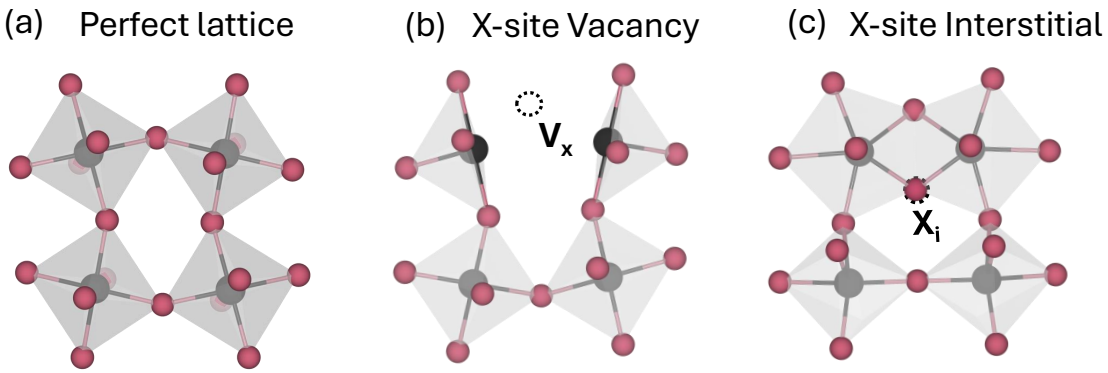

Figure 2.2: Schematic illustration of pristine halide perovskites and the corresponding vacancy and interstitial defects.

HPs contain a significant concentration of point defects, arising from synthesis conditions and their relatively low formation energies [16, 17, 45]. Many of these defects introduce shallow energy levels [27] and therefore do not strongly enhance non-radiative recombination [46], allowing long carrier diffusion lengths to be preserved [4, 28, 47]. Point defects are local deviations from the ideal crystal structure. In this thesis, the relevant defects are vacancies, where atoms are missing from lattice sites, and interstitials, where atoms occupy positions between lattice sites (see Figure 2.2). In ionic solids, these defects can be charged, and overall charge neutrality is maintained through a balance between compensating defects and electronic carriers [14, 16]. In $CsPbX_3$, halide vacancies are energetically favourable and can occur in high concentration under typical growth conditions [17, 48]. These defects play a key role in ionic transport [14, 39, 45]. A-site vacancies are associated with higher migration barriers and therefore contribute less to diffusion [14, 39].

Other defect types may also be present, depending on chemical environment. Interstitial defects become more relevant under halide-rich conditions, while antisite defects play a limited role in ionic transport. These considerations provide the basis for understanding defect-mediated ion migration, which is discussed in the next chapter.

2.4 CsPbX_3 as a model system

In this thesis, we focus on all-inorganic HPs of the form CsPbX_3 (X = I, Br, Cl), as well as mixed compositions $Cs_{1-x}Rb_xPbBr_{3(1-y)}I_{3y}$. These materials provide a suitable model system for studying ion migration due to their structural simplicity and compositional flexibility [6, 40]. In contrast to hybrid perovskites, CsPbX_3 does not contain molecular A-site cations. This removes additional degrees of freedom such as molecular rotation, hydrogen bonding, and dipolar interactions, allowing a more direct analysis of intrinsic ionic transport mechanisms.

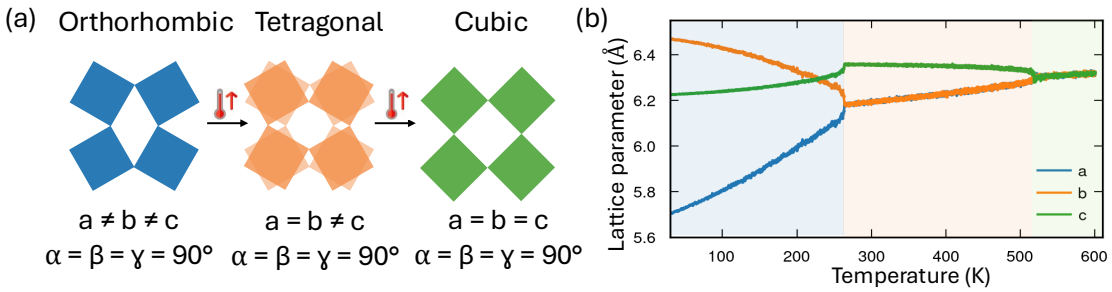

Figure 2.3: (a) Schematic illustration of the temperature-dependent phase transitions between orthorhombic, tetragonal, and cubic phases. (b) Lattice parameters as a function of temperature, showing the phase transitions from orthorhombic to tetragonal to cubic for $CsPbI_3$.

CsPbX_3 exhibits temperature-dependent phase transitions between orthorhombic, tetragonal, and cubic phases, as shown in Figure 2.3. At low temperatures, the orthorhombic phase (space group Pnma) is stable over a wide temperature range and serves as a the reference structure for first-principles calculations at 0 K. The higher-symmetry phases observed at higher temperatures can be interpreted as dynamical averages of locally distorted configurations [41, 49]. Compositional changes also affect the stability of different phases, for Br/I mixtures. In general, substitution of halides from I to Br to Cl reduces the ionic radius, leading to smaller lattice constants, stronger Pb–X bonding, and enhanced octahedral tilting [44]. Similarly, partial substitution of Cs with smaller cations such as Rb introduces additional lattice distortions. These structural variations influence both phase stability and defect energetics, and thereby affect ion migration through changes in the local atomic environment and lattice flexibility. These considerations provide the basis for the discussion of defect-mediated ion migration in the next chapter.

3

Defect-mediated ion migration

This chapter examines ion migration in HPs and its relation to material instability. The aim is to develop a physical understanding of defect-mediated ion motion, from underlying mechanisms to the key factors governing migration, with emphasis on halide transport in $CsPbX_3$.

3.1 Defect-mediated ion migration

Despite significant improvements in device performance, the long-term stability of perovskite solar cells remains limited. A major contributing factor is the intrinsic instability of the material, mediated by the presence and mobility of point defects [9, 13, 15, 22]. Ion migration occurs through thermally activated hopping between lattice sites, enabled by local disruptions of the periodic structure [50]. In HPs, ion migration is generally expected to occur predominantly via vacancy-mediated hopping, whereby neighboring ions move into vacant lattice sites, leading to the propagation of the vacancy through the lattice, as illustrated in Figure 3.1 [14]. Another possible pathway involves interstitial defects, in which ions occupy non-lattice positions [18]. At surfaces and grain boundaries, higher defect densities and lower coordination can further facilitate ionic transport [51]. Among the ionic species present, halide point defects are highly mobile, due to their relatively low migration barriers compared to A-site and B-site cations. In $CsPbX_3$, halide vacancies (V_X) are widely considered as the primary contributors to ionic transport due to their relatively high concentration and low migration barriers, typically reported in the range of $\sim$0.3–0.6 eV [17, 18, 51]. Interstitial defects are generally considered less important than vacancy-mediated migration under equilibrium conditions, but recent work suggests that low-energy interstitial pathways may contribute under halide-rich growth conditions [18, 52].

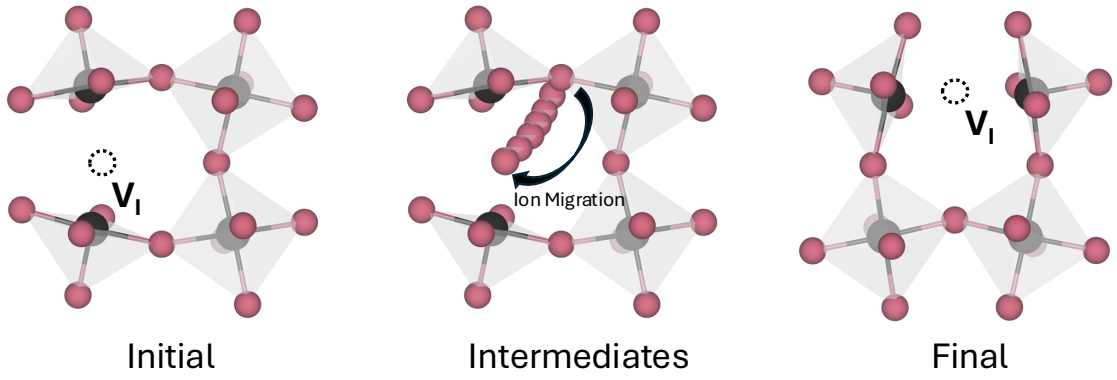

Figure 3.1: Schematic illustration of ion migration due to the presence of vacancy defects in the lattice.

The redistribution of ions within the lattice modifies the local composition and can alter the electronic properties of the material. In mixed-halide systems, this is associated with the formation of iodine-rich and bromine-rich regions under illumination [12, 35]. In devices, this contributes to current–voltage hysteresis, phase segregation and gradual performance degradation [11]. The accumulation of defects at surfaces and grain boundaries can further facilitate ionic transport and promote local structural changes [53]. These processes are influenced by external conditions such as illumination, and temperature, which enhance ionic mobility [37, 54–56].

3.2 Factors affecting ion migration

Ion migration depends on both the nature of defects and the local atomic environment. Electrostatic interactions and lattice distortions surrounding defects influence the energy landscape along the migration pathway and can modify the associated barriers [7, 15, 39]. Variation in composition and structure further affects this behaviour, particularly when comparing different halide species or crystallographic phases [18, 22, 48]. The local chemical environment and defect concentration also play a role, as they determine the availability of migration pathways and the interaction between defects. Thus, ion migration cannot be described by a single parameter, but reflects a combination of structural, chemical and environmental effects. This makes it difficult to establish consistent trends across different studies. In $CsPbX_3$, reported migration barriers vary significantly even for similar systems, indicating a strong sensitivity to both material and methodological factors [32, 39, 48].

3.3 Sensitivity of migration barriers to DFT methodology

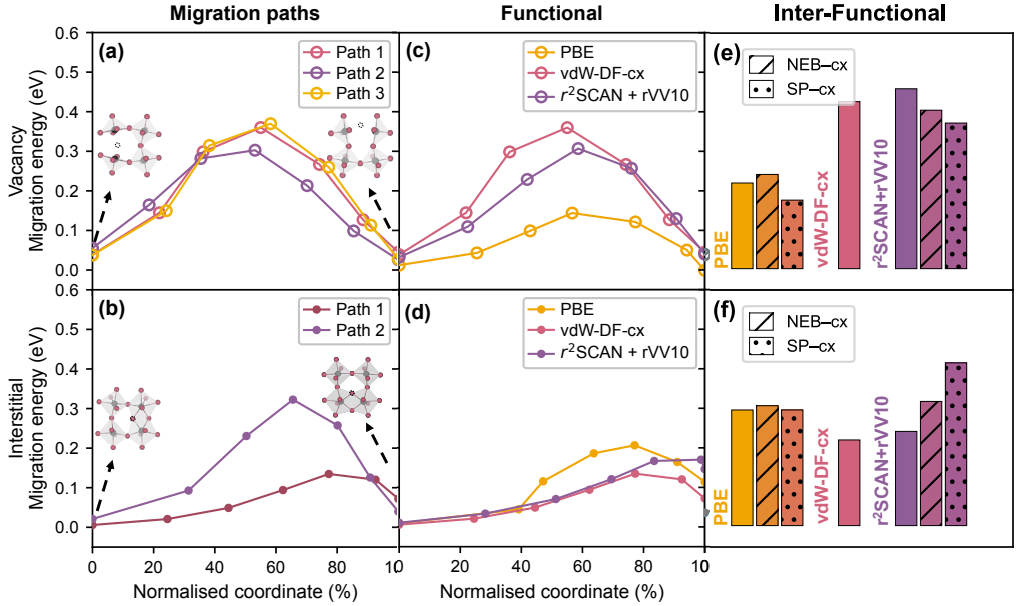

Figure 3.2: Halide-ion migration in orthorhombic $CsPbI_3$ computed using the vdW-DF-cx functional. (a,b) Migration energy profiles for vacancy (V_I) and interstitial (I_i) mechanisms along different diffusion pathways; path 1 (inset) is used as the reference. (c,d) Functional dependence of migration barriers along path 1. (e,f) Inter-functional volume tests for V_I^+ and I_i^-: NEB-cx denotes vdW-DF-cx barriers from fixed-volume NEB calculations (endpoints re-relaxed at PBE or r^{2}SCAN+rVV10 volumes), while SP-cx denotes single-point vdW-DF-cx energies evaluated along paths obtained with PBE or r^{2}SCAN+rVV10. Open and filled circles represent vacancy and interstitial mechanisms, respectively. The reaction coordinate Q is normalized from 0% (initial state) to 100% (final state). *Adapted from Paper I.*

Ion migration in $CsPbX_3$ has been widely studied, yet reported migration barriers show considerable variation across the literature due to methodological choices. For iodide vacancies in $CsPbI_3$, PBEsol calculations give a barrier of ∼0.34 eV for V_I^+ [57], while PBE-D3-BJ yields a higher value of ∼0.44 eV for the same defect and charge state [20]. A similar sensitivity is observed in $CsPbBr_3$, PBE/NEB calculations report a bulk V_{Br} barrier of ∼0.58 eV [51], whereas PBE/NEB calculations in the orthorhombic phase give lower values of 0.23–0.34 eV depending on the migration pathway [58]. Barriers also depend on the defect charge state, increasing from ∼0.34 eV for V_I^+ to ∼0.45–0.50 eV for V_I^0 and V_I^- respectively, in $CsPbI_3$ [57]. The inclusion of spin–orbit coupling (SOC) further modifies defect energetics and can shift migration barriers [27, 59, 60].

In addition to methodological choices, physical factors such as halide composition, migration pathway, and local environment also contribute to the observed variations [15, 61]. For example, migration in $CsPbI_3$ is generally faster than in $CsPbBr_3$, consistent with a weaker Pb–I bonding [18]. Surface environments can lower migration barriers compared to bulk systems, and interstitial pathways may become competitive under certain growth conditions [18, 51, 52]. The variations in migration barriers reported in the literature therefore arise from a combination of methodological choices and physical differences, including the exchange–correlation functional, defect charge state, migration pathway, local structure, and lattice volume. As a result, it becomes difficult to directly compare results across different studies and to establish consistent trends. This highlights the need for systematic and consistent benchmarking of migration barriers.

In Paper I, we address this by analysing how migration barriers depend on different computational choices using DFT-based NEB calculations. We first compute halide vacancy- and interstitial- mediated migration barriers in orthorhombic $CsPbI_3$, assess the influence of distinct migration pathways and defect charge state, and compare multiple exchange–correlation functionals (PBE, vdW-DF-cx, r^{2}SCAN+rVV10, vdW-DF-cx with spin-orbit coupling, and the hybrid functional PBE0). To separate structural (volume/geometry) effects from energetic evaluation along the path, we also perform inter-functional tests by evaluating migration energetics with vdW-DF-cx on structures relaxed using PBE and r^{2}SCAN+rVV10. The results are discussed in Paper I and adapted in Figure 3.2. Across the tested setups, migration barriers vary by up to 0.38 eV. The inter-functional tests show that most of this spread occurs due to functional-dependent lattice volumes and the resulting local steric environment at the transition state. Vacancy and interstitial mechanisms respond differently to structure compactness, leading to opposite volume trends. Extending our analysis across the different halides (X = Cl, Br, I) shows a decrease in vacancy barrier from iodide to chloride, suggesting a balance between the halide ion size and lattice volume; interstitial trends are less monotonic and more sensitive to local transition-state stabilization. These results provide a benchmark for assessing method sensitivity in DFT migration barriers and for using them more consistently in ion-diffusion and stability studies of HPs.

While these calculations resolve individual migration events at the atomic scale, they are limited to relatively small system sizes and short time scales. In real materials, ion transport depends on defect concentration, defect interactions and collective effects, as well as temperature requiring approaches that extend beyond individual migration processes, as discussed in the next chapter.

4

Ion diffusion in mixed $Cs_{1-x}Rb_xPbBr_{3(1-y)}I_{3y}$ Perovskites

This chapter presents ion diffusion in mixed HPs $Cs_{1-x}Rb_xPbBr_{3(1-y)}I_{3y}$. The focus is on understanding how compositional variations influence ionic transport at finite temperatures. In contrast to the description of individual migration events in Chapter 3 and Paper I, diffusion is treated here as a collective and temperature-dependent process, providing a direct connection between atomistic migration mechanisms and macroscopic transport behavior.

4.1 Introduction to diffusion

In the previous chapter, ion migration was described as defect-mediated hopping between lattice sites and the associated migration barriers. These barriers describe individual hopping events, but ion transport in real materials does not occur through a single hop; rather, it occurs through the accumulation of many such events over time. At the macroscopic level, diffusion is described by Fick's law, where a concentration gradient gives rise to a particle flux $\mathbf{J} = -D\nabla c$, where $\mathbf{J}$ is the particle flux, D is the diffusion coefficient, and c is the local concentration. This macroscopic behavior originates from atomic motion in the lattice. At the atomic scale, diffusion arises from the thermally activated stochastic motion of atoms or ions through successive displacements. In solids, this motion occurs through defects, such as vacancies or interstitials, which enable atoms to hop between lattice sites as shown by the schematic in Figure 4.1 [14]. Repeated hopping over time leads to long-range transport.

In atomistic simulations, diffusion is quantified using the mean squared displacement

(MSD), which measures how far a particle moves on average over time [62],

$$\mathrm{MSD}(t) = \left\langle \left| \mathbf{r}_i(t) - \mathbf{r}_i(0) \right|^2 \right\rangle, \tag{4.1}$$

where $\mathbf{r}_i(t)$ is the position of particle i at time t, and the average is taken over all particles and different time origins. At short simulation times, the motion is not diffusive

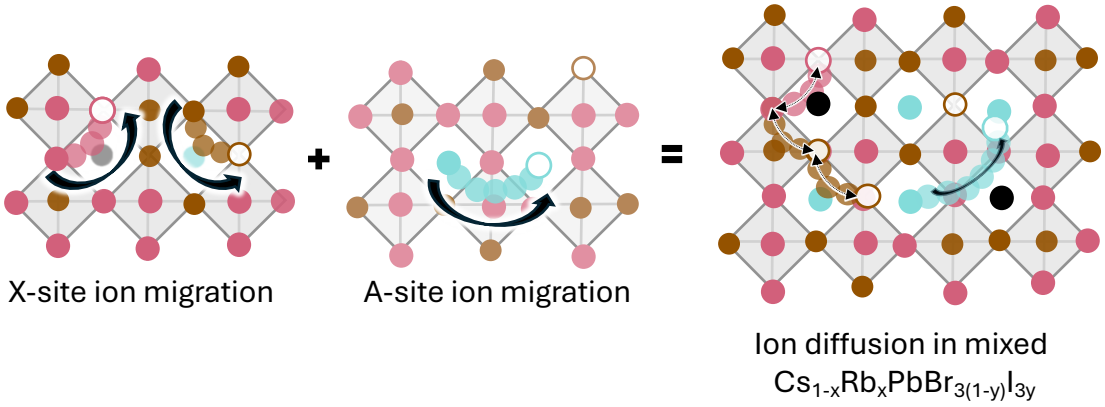

Figure 4.1: Schematic illustration of vacancy-mediated ion migration and diffusion. The left panel shows X-site vacancy-driven migration of halide ions, the middle panel illustrates A-site vacancy-driven migration of A-site cations, and the right panel presents collective ion diffusion at elevated temperature, involving simultaneous migration of multiple X- and A-site ions in mixed $Cs_{1-x}Rb_xPbBr_{3(1-y)}I_{3y}$.

and instead reflects local non-diffusive motion. At sufficiently long times, the motion becomes diffusive and the MSD increases linearly with time. In practice, the diffusion coefficient D is obtained from the slope of the linear region of the MSD using the Einstein relation [62],

$$D = \lim_{t\to\infty} \frac{1}{6t} \left\langle |\mathbf{r}(t) - \mathbf{r}(0)|^2 \right\rangle. \tag{4.2}$$

Ion diffusion reflects the cumulative effect of many migration events and depends on migration barriers, defect concentrations, temperature, and the local lattice environment [9, 13, 14]. A study based only on individual migration barriers is therefore not sufficient, and it becomes necessary to consider transport at larger length and time scales [15]. In defect-mediated systems such as HPs, ion motion is controlled by the concentration of defects and the associated migration barriers. In mixed systems, such as $CsPbBr_{3(1-y)}I_{3y}$, diffusion can vary significantly with composition. Changes in halide and A-site composition modify lattice parameters, bonding, and local disorder, which can affect both the hopping process and the overall diffusion coefficient [18, 63]. Collective effects arising from composition and lattice dynamics are therefore captured through MSD-based analysis rather than relying only on individual migration barriers.

4.2 Ion diffusion described by the Arrhenius equation

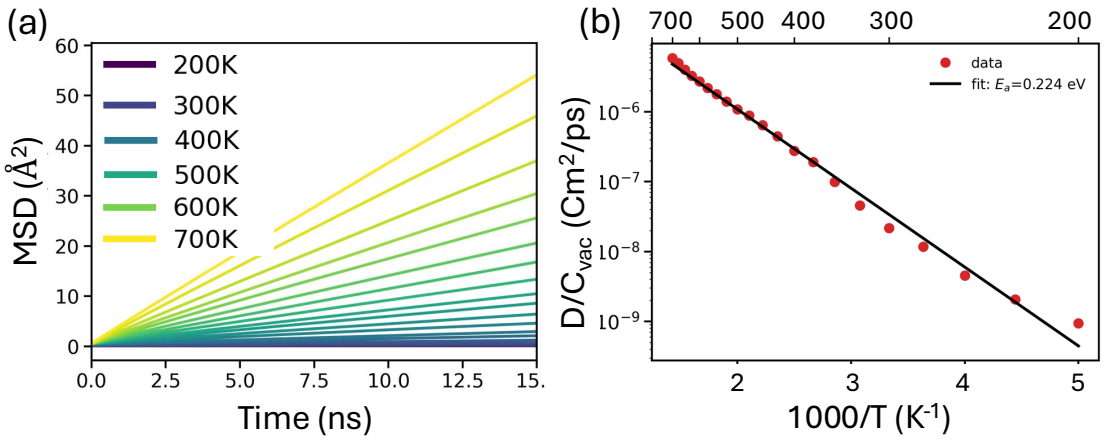

Figure 4.2: Ion diffusion analysis workflow from MD simulations: (a) MSD as a function of time, (b) diffusion coefficients extracted from the MSD at different temperatures, followed by Arrhenius analysis by plotting ln D versus $1000/T$ to determine the activation energy and prefactor of $CsPbBr_3$.

In solids, the temperature dependence of diffusion is described by an Arrhenius-type relation,

$$D = D_0 \exp\left(-\frac{E_a}{k_B T}\right), \tag{4.3}$$

where D_0 is the prefactor and E_a is the activation energy. This expression shows that diffusion is a thermally activated process, with the exponential term describing how rapidly the diffusion coefficient increases with temperature.

For defect-mediated ion diffusion, this relation can be understood in terms of microscopic processes involving a sequence of atomic jumps between lattice sites. The diffusion coefficient can be written as

$$D = \frac{1}{2d} f\, z\, \nu\, a^2 \exp\left(-\frac{E_a}{k_B T}\right), \tag{4.4}$$

where z is the number of equivalent jump directions (coordination number) and d is the dimensionality of diffusion. ν is the attempt frequency, a is the jump distance, and f is the correlation factor. The jump distance is typically of the order of the nearest-neighbor spacing, $a \approx a_0$, which directly reflects the crystal structure.

The exponential term $\exp(-E_a/k_B T)$ represents the probability that an ion can overcome the migration barrier due to thermal activation. Because of its exponential form,

this term dominates diffusion, such that even small changes in E_a lead to large changes in D. As a result, migration barriers obtained from atomistic calculations play a central role in determining diffusion behavior. The activation energy E_a reflects the energy required for atomic motion and is related to the migration barrier. In intrinsic diffusion, it is expressed as $E_a = E_f + E_m$, where E_f is the defect formation energy and E_m is the migration barrier. In HPs, defects can be present in relatively high concentrations and may not strictly follow equilibrium thermodynamics over the temperature range considered. As a result, diffusion is often dominated by the migration component, and an effective activation energy close to E_m is observed when defect concentrations vary weakly with temperature [14, 16]. The activation energy obtained from diffusion measurements represents an effective barrier for long-range transport, which may differ from the local migration barrier due to collective effects and defect interactions. The activation energy E_a depends on several factors, including local atomic structure, bonding strength (Pb–X interaction), crystal phase, and chemical composition such as Br/I or Cs/Rb substitution [18, 21].

The prefactor D_0 captures the dynamical aspects of diffusion and can be approximated as $D_0 \sim \frac{1}{2d} f z \nu a^2$, where ν is the attempt frequency, a is the jump distance, z is the number of equivalent jump directions, d is the dimensionality, and f is the correlation factor [15]. The attempt frequency ν is related to lattice vibrations and phonon frequencies, linking lattice dynamics to diffusion [64]. The jump distance a depends on the underlying lattice geometry. Atomic jumps are not completely independent, and the correlation factor f accounts for short-range correlations in successive jumps. In vacancy-mediated diffusion, an atom that moves into a vacancy has a finite probability of returning to its original site. Such back-and-forth motion does not contribute to net transport and reduces the effective diffusion coefficient. The correlation factor captures this effect and depends on the diffusion mechanism and crystal structure. However, it does not describe long-range collective motion, which can become relevant in soft lattices.

In HPs, the lattice is soft and exhibits significant anharmonicity, characterized by low-frequency vibrational modes and large atomic displacements [7, 8]. The prefactor therefore contains information about lattice dynamics and structural flexibility. The overall diffusion coefficient is determined by a combination of the exponential term, which governs the dominant temperature dependence, and the prefactor, which includes lattice dynamics, jump geometry, and correlation effects. Systems with similar activation energies can still exhibit differences in diffusion due to variations in the prefactor. This is particularly relevant when comparing A-site and X-site substitutions. While Br/I mixing primarily raises migration barriers, Rb incorporation stiffens the lattice and modifies the attempt frequency, influencing the prefactor. Thus studying the interplay between these mechanisms across the compositional space of $Cs_{1-x}Rb_xPbBr_{3(1-y)}I_{3y}$ is important to understand [18, 63, 64].

4.3 Modeling ion diffusion in mixed halide perovskites

The diffusion processes described above can be studied in atomistic simulations by following atomic motion over time. Static first-principles calculations based on DFT are limited to relatively small systems, and first-principles MD is further restricted to short time scales. MD simulations provide a natural framework for studying ion diffusion at finite temperature by explicitly evolving atomic trajectories [15]. However, when the forces are computed directly from DFT, the computational cost remains too high for the large systems and long simulation times required to study diffusion. To overcome this limitation, MLIPs trained on DFT data have emerged as an efficient approach [18]. Using MLIPs, MD simulations can be performed on larger supercells and over longer time scales while retaining near-DFT accuracy. The resulting atomic trajectories are then used to calculate the MSD as shown in Figure 4.2a, from which the diffusion coefficient is extracted at each temperature. By performing simulations across a range of temperatures, the temperature dependence of the diffusion coefficient can be analysed and related to the Arrhenius behaviour described above as shown in Figure 4.2b.

4.4 Effect of composition on ion diffusion

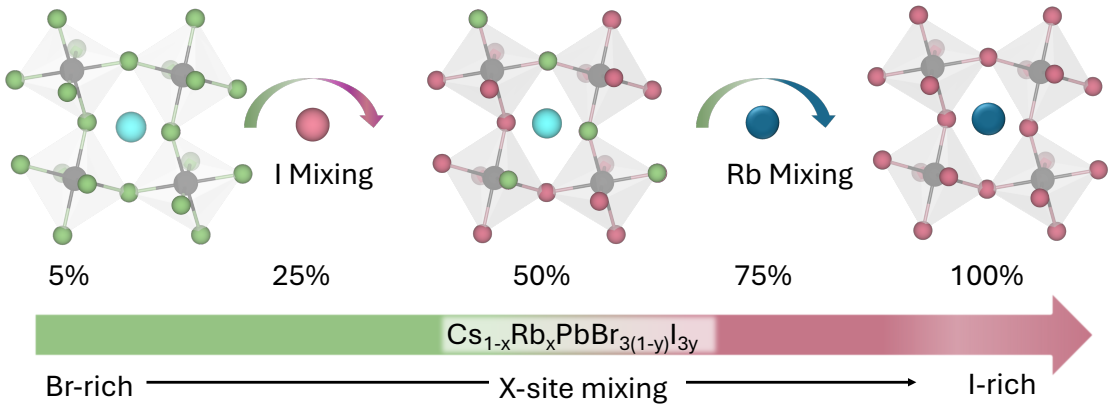

Figure 4.3: Schematic illustration of compositional substitution in $Cs_{1-x}Rb_xPbBr_{3(1-y)}I_{3y}$, showing halide substitution from Br (green) to larger I (pink) and replacement of the A-site cation Cs (cyan) by smaller Rb (blue). The iodide fraction varies from $y = 0\%$ to 100%, while the Rb concentration varies from $x = 0\%$ to 30%.

In mixed HPs, compositional engineering is widely used to tune material properties and improve stability. Mixing at X-site and A-site modifies the lattice structure, local distortion and lattice dynamics and therefore also influence the ion transport.

This makes mixed compositions relevant model systems for studying how composition affects diffusion [13, 15]. Schematic illustration of compositional substitution in $Cs_{1-x}Rb_xPbBr_{3(1-y)}I_{3y}$, showing halide substitution from Br to larger I (from $y = 0\%$ to 100%) and replacement of the A-site cation Cs by smaller Rb (from $x = 0\%$ to 30%) as shown in Figure 4.3. The mixed-cation and mixed-HPs are actively studied in high-efficiency photovoltaic materials, where ion migration and phase stability remain central challenges [13, 15, 65]. Substitution of Cs by the smaller Rb cation modifies the lattice and can stabilize the high-symmetry perovskite phase, while also affecting lattice dynamics [64]. Substitution of bromine with iodine leads to a less compact lattice and weaker Pb–X bonding, which influence migration barriers [18, 21]. Together, these substitutions provide a controlled way to tune both the structural and dynamical factors governing ion diffusion, which motivates the study of mixed $Cs_{1-x}Rb_xPbBr_{3(1-y)}I_{3y}$ system.

The $CsPbX_3$ family exhibits temperature-dependent phase transitions between cubic, tetragonal, and orthorhombic phases as shown in Figure 2.3b [41]. These structural changes influence ion transport, as high-symmetry phases provide more direct migration pathways, while lower-symmetry phases introduce distortions that hinder atomic motion [15]. Near phase transitions, the lattice becomes softer and shows enhanced dynamical fluctuations [7, 41]. In mixed compositions, these effects are further modified by local chemical variations, which can leads to multiple diffusion pathways and possible deviations from ideal Arrhenius behaviour [13, 18].

In this work, the diffusion coefficient $\boldsymbol{D}$ is obtained from the MSD, and the activation energy $\boldsymbol{E_a}$ is extracted from its temperature dependence. In Paper II, diffusion is systematically analysed across the compositional space of $Cs_{1-x}Rb_xPbBr_{3(1-y)}I_{3y}$ using NEP-based MD simulations. The compositional space is spanned systematically across $x = 0, 10, 20, 30\%$ and $y = 0, 5, \ldots, 95, 100\%$ in $Cs_{1-x}Rb_xPbBr_{3(1-y)}I_{3y}$. To do this, NEP-based ML interatomic potentials are trained to perform large-scale MD simulations, allowing to study the effect of halide and A-site mixing on $\boldsymbol{E_a}$ and $\boldsymbol{D_0}$ to be mapped systematically. In Paper III, selected compositions are studied in collaboration with experiments, including $CsPbBr_3$, $Cs_{0.75}Rb_{0.25}PbBr_3$, $CsPbBr_{1.5}I_{1.5}$, and $Cs_{0.75}Rb_{0.25}PbBr_{1.5}I_{1.5}$, allowing direct comparison between atomistic simulations and experimentally observed ion dynamics.

5

Computational methods

The physics of ion diffusion and migration mechanisms has been discussed in the previous chapters, and this chapter describes how these quantities are computed. The calculations combine first-principle, DFT, the NEB method, NEP based MLIP, and MD. DFT provides the energetics, NEB gives migration barriers, and MLIP enable large-scale MD simulations at finite temperature.

5.1 First-principles methods

At the most fundamental level, a material is described as a quantum mechanical many-body system consisting of interacting electrons and atomic nuclei. Its properties are obtained by solving the non-relativistic time-independent Schrödinger equation,

$$\hat{H}\Psi(\mathbf{R},\mathbf{r}) = E\Psi(\mathbf{R},\mathbf{r}), \tag{5.1}$$

where $\Psi(\mathbf{R},\mathbf{r})$ depends on the nuclear coordinates $\mathbf{R}$ and electronic coordinates $\mathbf{r}$. The Hamiltonian $\hat{H}$ includes the kinetic energies of electrons and nuclei, as well as all Coulomb interactions, and can be written as $\hat{H} = T_n + T_e + V_{ne} + V_{ee} + V_{nn}$, where T_n and T_e are the kinetic energies of nuclei and electrons, and V_{ne}, V_{ee}, and V_{nn} represent the electron–nucleus, electron–electron, and nucleus–nucleus interactions. However, for realistic systems, this equation cannot be solved exactly because the motion of all particles is coupled.

The Born–Oppenheimer approximation is introduced to make the problem tractable by taking into account the large mass difference between nuclei and electrons ($m_\mathrm{n} \gg m_\mathrm{e}$). Thus, the nuclei are treated as fixed, and the electronic problem is solved for a given atomic configuration. This leads to the electronic Schrödinger equation,

$$\hat{H}_e\Psi_e(\mathbf{r};\mathbf{R}) = \epsilon(\mathbf{R})\Psi_e(\mathbf{r};\mathbf{R}), \tag{5.2}$$

where $\epsilon(\mathbf{R})$ represents the energy of the system for a given atomic configuration. This energy defines the potential-energy surface used to compute forces and atomic motion.

5.2 Density Functional Theory (DFT)

Electron–electron interactions make the direct solution of the above electronic Schrödinger equation impractical for realistic systems. DFT is introduced to make the problem tractable. In DFT, the system is described using the electron density $n(\mathbf{r})$ instead of the many-body wavefunction [66]. The Hohenberg–Kohn theorems show that the ground-state energy is a functional of the density, and the ground-state density minimizes the energy functional,

$$E[n] = F[n] + \int V_{\text{ext}}(\mathbf{r})\, n(\mathbf{r})\, d\mathbf{r}, \tag{5.3}$$

where $F[n]$ is a universal functional and $V_{\text{ext}}(\mathbf{r})$ is the external potential. However, these theorems are valid only for ground-state properties and do not provide the explicit form of the energy functional.

The Kohn–Sham formulation is introduced to make the problem tractable. It replaces the interacting system of real electrons with an auxiliary system of non-interacting particles that reproduces the same ground-state density as the real system. The electron density is written as

$$n(\mathbf{r}) = \sum_i f_i |\phi_i(\mathbf{r})|^2, \tag{5.4}$$

where $\phi_i(\mathbf{r})$ are the Kohn–Sham orbitals. These are obtained by solving

$$\left[-\frac{\hbar^2}{2m}\nabla^2 + V_{\text{KS}}(\mathbf{r})\right] \phi_i(\mathbf{r}) = \varepsilon_i \phi_i(\mathbf{r}), \tag{5.5}$$

with the effective potential

$$V_{\text{KS}}(\mathbf{r}) = V_{\text{ext}}(\mathbf{r}) + V_{\text{H}}(\mathbf{r}) + V_{\text{xc}}(\mathbf{r}) = V_{\text{ext}}(\mathbf{r}) + \int \frac{n(\mathbf{r}')}{|\mathbf{r} - \mathbf{r}'|}\, d\mathbf{r}' + \frac{\delta E_{\text{xc}}[n]}{\delta n(\mathbf{r})} \tag{5.6}$$

Here, $V_{\text{H}}(\mathbf{r})$ is the Hartree potential, which accounts for the classical electron–electron repulsion, and $V_{\text{xc}}(\mathbf{r})$ includes all many-body exchange and correlation effects.

The total energy functional in the Kohn–Sham framework is written as

$$E[n] = T_s[n] + \int V_{\text{ext}}(\mathbf{r}) n(\mathbf{r})\, d\mathbf{r} + \frac{1}{2}\int\int \frac{n(\mathbf{r})n(\mathbf{r}')}{|\mathbf{r} - \mathbf{r}'|}\, d\mathbf{r}\, d\mathbf{r}' + E_{\text{xc}}[n], \tag{5.7}$$

where $T_s[n]$ is the kinetic energy of the non-interacting reference system and $E_{\text{xc}}[n]$ contains all many-body contributions beyond the classical electrostatic term.

The Kohn–Sham equations are solved self-consistently. An initial guess for the electron density is made, from which the effective potential is constructed, and the equations are solved to obtain a new density. This updated density is then compared with the previous one. The process is repeated, with the potential and orbitals updated at each step, until convergence of the total energy and charge density is achieved. Although this procedure determines the final electron density, the exact exchange–correlation functional remains unknown.

5.2.1 Exchange–correlation functionals

The accuracy of DFT calculations depends on the choice of exchange–correlation functional. Since the exact form of the exchange–correlation energy $E_{\mathrm{xc}}[n]$ is not known, different approximations are used.

In the local density approximation (LDA), the electron density at each point is assumed to behave like a homogeneous electron gas, and the exchange–correlation energy depends only on the local density,

$$E_{\mathrm{xc}}^{\mathrm{LDA}}[n] = \int n(\mathbf{r})\, \varepsilon_{\mathrm{xc}}^{\mathrm{hom}}(n(\mathbf{r}))\, d\mathbf{r}. \tag{5.8}$$

This approximation works well when the density varies slowly, but it overestimates bond strengths and underestimates bond lengths [67].

The generalized gradient approximation (GGA) includes the spatial variation of the density, so the exchange–correlation energy depends on both the density and its gradient,

$$E_{\mathrm{xc}}^{\mathrm{GGA}}[n] = \int n(\mathbf{r})\, \varepsilon_{\mathrm{xc}}(n(\mathbf{r}), \nabla n(\mathbf{r}))\, d\mathbf{r}. \tag{5.9}$$

This gives better results for systems where the density changes more rapidly [68]. The choice of exchange–correlation functional is important for HPs, where lattice softness, relativistic effects, cation off-centering, and long-range interactions influence phase transitions, defect energetics and migration barriers. Many functionals are available, and their performance depends on the system being studied. In Paper I, we systematically analyse the sensitivity of migration barriers to the choice of exchange–correlation functional, enabling consistent comparison across $CsPbX_3$ systems.

5.2.1.1 Perdew–Burke–Ernzerhof (PBE)

PBE is used as a standard GGA functional, with the exchange–correlation energy expressed as

$$E_{\mathrm{xc}}^{\mathrm{PBE}}[n] = \int n(\mathbf{r})\, \varepsilon_{\mathrm{xc}}^{\mathrm{PBE}}(n(\mathbf{r}), \nabla n(\mathbf{r}))\, d\mathbf{r}. \tag{5.10}$$

PBE is widely used because it gives a reasonably good description of structures and energies without the need for system-specific parameters [69].

5.2.1.2 r^{2}SCAN+rVV10

The meta-GGA functional r^{2}SCAN includes the kinetic energy density (τ) and improves the description of bonding. Its exchange–correlation energy is written as

$$E_{\mathrm{xc}}^{\mathrm{r^2SCAN}}[n, \nabla n, \tau] = E_x^{\mathrm{r^2SCAN}}[n, \nabla n, \tau] + E_c^{\mathrm{r^2SCAN}}[n, \nabla n, \tau]. \tag{5.11}$$

Including τ helps to describe bonding more accurately and improves numerical stability [70]. To account for dispersion interactions, r^{2}SCAN is combined with the nonlocal rVV10 correction,

$$E_c^{\mathrm{rVV10}}[n] = \int n(\mathbf{r})\, \Phi[n](\mathbf{r})\, d\mathbf{r}, \tag{5.12}$$

where $\Phi[n]$ represents a nonlocal term that captures long-range interactions [71]. This is important for systems where van der Waals forces play a role [72].

5.2.1.3 vdW-DF-cx

The vdW-DF-cx functional is used to include nonlocal van der Waals interactions directly. The exchange–correlation energy is written as

$$E_{\mathrm{xc}}^{\mathrm{vdW-DF-cx}} = E_x^{\mathrm{cx}} + E_c^{\mathrm{LDA}} + E_c^{\mathrm{nl}}, \tag{5.13}$$

where E_c^{nl} is the nonlocal correlation term. This functional is useful for systems where long-range interactions are important [73].

5.2.1.4 PBE0

The hybrid functional PBE0 mixes exact exchange with GGA exchange,

$$E_{\mathrm{xc}}^{\mathrm{PBE0}} = \alpha E_x^{\mathrm{HF}} + (1 - \alpha) E_x^{\mathrm{PBE}} + E_c^{\mathrm{PBE}}. \tag{5.14}$$

where $\alpha = 0.28$ is used in Paper I.

5.3 Climbing image nudged elastic band (CI-NEB) method

The NEB method is used to find the minimum energy path (MEP) between two stable configurations and to estimate the corresponding activation energy [19]. The MEP is the most likely path the system follows at 0 K when moving from one state to another, such as during ion migration. In NEB, the path between the initial and final states is represented by a series of intermediate configurations, called images. These images are snapshots of the system along the transition path. They connect the two end points and

describe how the system evolves step by step. To keep the images properly distributed along the path, they are connected by artificial spring forces, which prevent them from collapsing toward the end points. The schematic illustration of the NEB method for calculating migration barriers is shown in Figure 5.1. During the optimization, the force acting on each image is split into two parts: one along the path and one perpendicular to it. The true force from the potential energy surface acts only in the perpendicular direction and pushes the images toward the minimum energy path. The artificial spring force acts only along the path and keeps the images evenly spaced. This separation of forces is known as nudging and helps the path converge smoothly.

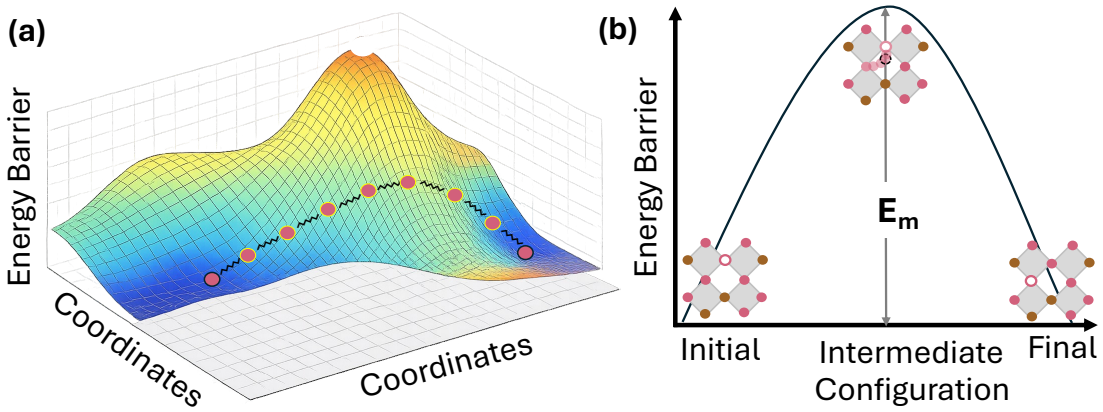

Figure 5.1: Schematic illustration of the NEB method for calculating migration barriers. a) The potential energy surface (PES) with a discrete set of intermediate images (red circles) connecting the initial and final states, representing the minimum energy path. The highest point along the path corresponds to the saddle point. b) The corresponding atomic migration pathway, where the activation energy E_m is defined as the energy difference between the saddle point and the initial state.

For a band consisting of $N+1$ images, the initial and final configurations $\mathbf{R}_0$ and $\mathbf{R}_N$ are kept fixed. The force acting on an intermediate image i is written as

$$\mathbf{F}_i^{\mathrm{NEB}} = \mathbf{F}_i^{\perp} + \mathbf{F}_i^{S,\parallel}, \tag{5.15}$$

where S denotes the spring force and $\parallel$ indicates the component along the path. The perpendicular component of the true force and is

$$\mathbf{F}_i^{\perp} = -\nabla E(\mathbf{R}_i) + \big[\nabla E(\mathbf{R}_i)\cdot\boldsymbol{\tau}_i\big]\boldsymbol{\tau}_i, \tag{5.16}$$

where $\boldsymbol{\tau}_i$ is the unit tangent vector to the path at image i and the parallel component of the spring force is

$$\mathbf{F}_i^{S,\parallel} = k\big(|\mathbf{R}_{i+1}-\mathbf{R}_i| - |\mathbf{R}_i-\mathbf{R}_{i-1}|\big)\boldsymbol{\tau}_i. \tag{5.17}$$

where k is the spring constant and $\boldsymbol{\tau}_i$ is the unit tangent to the path at image i.

To obtain a better estimate of the transition state, the climbing image NEB (CI-NEB) method is used [19]. In this approach, the image with the highest energy is pushed directly toward the saddle point by modifying the force along the path. The force acting on this image is given by

$$\mathbf{F}_l^{\mathrm{CI}} = -\nabla E(\mathbf{R}_l) + 2\big[\nabla E(\mathbf{R}_l) \cdot \boldsymbol{\tau}_l\big]\boldsymbol{\tau}_l. \tag{5.18}$$

This approach drives the image toward the saddle point, corresponding to the highest energy along the migration path [74].

This method provides migration barriers for ion transport [14, 20]. In Paper I, the CI-NEB method is used to determine migration pathways and activation energies for defect-induced ion migration in $CsPbX_3$.

5.4 Molecular dynamics (MD)

The material behavior at finite temperature can be quite different from that at 0 K because of thermal motion and interactions between atoms. DFT can give accurate ground-state properties, but it does not directly describe how atoms move with time or how diffusion happens. MD is used to study these effects by following the atomic motion explicitly. In MD, atoms move according to Newton's equations of motion [62]. The force acting on atom I at time t is given by

$$\mathbf{F}_I(t) = -\nabla_I U\big(\mathbf{R}(t)\big), \tag{5.19}$$

where $U(\mathbf{R}(t))$ is the potential energy of the system and $\mathbf{R}(t)$ represents the set of atomic positions.

The time evolution of atom I is described by its position and velocity, which are propagated in time using a small time step Δt. Using Newton's second law, the velocity and acceleration are given by

$$\mathbf{v}_I(t) = \frac{d\mathbf{r}_I(t)}{dt}, \tag{5.20}$$

$$\mathbf{a}_I(t) = \frac{d\mathbf{v}_I(t)}{dt} = \frac{\mathbf{F}_I(t)}{m_I}. \tag{5.21}$$

In practice, these equations cannot be solved analytically for a many-body system, so numerical methods are used. An integrator is used to solve these equations in a stable and accurate way, while minimizing numerical errors.

A widely used integrator is the velocity Verlet algorithm [75], which is stable and conserves energy well over long simulation times. The positions are updated as

$$\mathbf{R}_I(t + \Delta t) = \mathbf{R}_I(t) + \mathbf{v}_I(t)\Delta t + \frac{1}{2}\frac{\mathbf{F}_I(t)}{m_I}\Delta t^2, \tag{5.22}$$

After updating the positions, the forces at the new positions, $\mathbf{F}_I(t + \Delta t)$, are calculated, and the velocities are updated as

$$\mathbf{v}_I(t + \Delta t) = \mathbf{v}_I(t) + \frac{1}{2}\left[\frac{\mathbf{F}_I(t)}{m_I} + \frac{\mathbf{F}_I(t + \Delta t)}{m_I}\right]\Delta t. \tag{5.23}$$

Repeating these updates generates the atomic trajectory over time. The choice of time step is a compromise between accuracy and computational cost. A large time step can lead to inaccuracies or instability, while a small time step increases the computational cost.

Time propagation using the velocity verlet algorithm can be carried out in different statistical ensembles, depending on the conditions being studied. In the NVE ensemble, the number of atoms, volume, and energy are fixed. In the NVT ensemble, the temperature is controlled, and in the NPT ensemble, both temperature and pressure are controlled [76].

In practice, simulations start from an initial structure obtained from DFT or experimental insights. This structure is first equilibrated to reach the desired temperature and pressure. A common approach is to use NPT for equilibration and then use the final configuration to perform NVT or NVE simulations, depending on the property of interest. NVT is useful when properties at a fixed temperature are required, while NVE is often preferred for studying dynamical properties because it does not introduce additional forces from thermostats or barostats.

The production run then generates the atomic trajectory used for further analysis. From this trajectory, properties such as ion diffusion can be calculated. In particular, ion diffusion is characterized through the MSD, from which the diffusion coefficient is extracted. The temperature dependence of the diffusion coefficient is then analyzed using the Arrhenius relation to obtain activation energies. This connects atomic motion to macroscopic transport and supports the results obtained from DFT.

5.5 Machine-learned interatomic potentials

DFT calculations are performed on relatively small supercells, as system sizes beyond a few hundred atoms become prohibitively expensive. Although periodic boundary conditions are used to represent bulk behavior, finite-size effects can still be important. Capturing disorder, defect interactions, and long-range diffusion therefore requires significantly larger systems than are accessible with direct DFT. In principle, MD can be performed directly using DFT, but the computational cost is very high. This limits both the accessible system sizes and simulation times, making it difficult to study processes such as diffusion that require large systems and long time scales. There is therefore a need for approaches that retain DFT accuracy while allowing more efficient simulations.

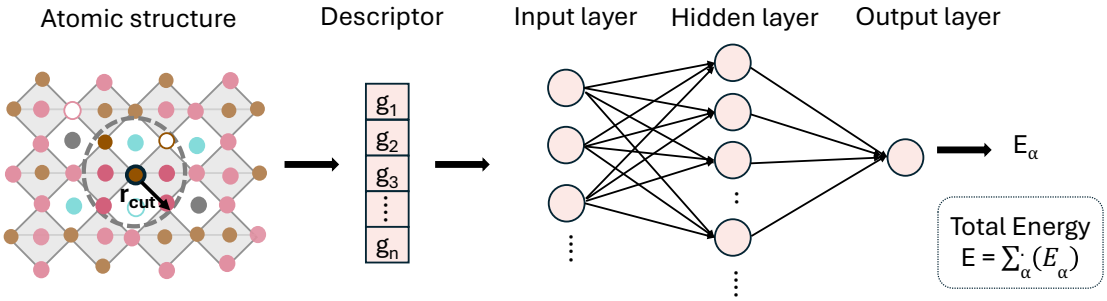

Figure 5.2: Schematic illustration of the NEP-based MLIP. The local atomic environment around a reference atom α, defined a cutoff radius r_{cut}, is mapped onto a set of invariant descriptors $(g_1, g_2, \ldots, g_n)$. These descriptors are used as input to feed-forward neural network, which predicts the atomic energy contribution E_α. The total energy of the system is obtained as a sum over all atomic energies.

Recent advances in ML have made it possible to construct interatomic potentials with near-DFT accuracy at a much lower computational cost. These MLIPs enable simulations of significantly larger systems over longer time scales compared to direct DFT-based MD. This is particularly important for studying diffusion, where both system size and simulation time play a critical role. In this way, MLIPs provide a bridge between accurate first-principles calculations and efficient MD simulations. In Papers II and III, a MLIP based on the fourth generation NEP framework is developed[77, 78] using the iterative procedure described in previous study [41]. The idea is to learn the potential energy surface directly from DFT data. Instead of solving the electronic structure problem at every time step, the model predicts energies and forces based on the local atomic environment.

In NEP, the total energy of the system is expressed as a sum of atomic contributions,

$$E_{\text{total}} = \sum_i E_i, \tag{5.24}$$

where each atomic energy E_i depends on the local environment of atom i. This assumption is used because the interaction of an atom is primarily determined by its neighboring atoms within a finite cutoff distance. To describe the local environment, a set of descriptors is constructed for each atom. The NEP descriptors consist of both radial (interatomic distances) and angular (relative atomic arrangements) components. Also, these descriptors are invariant with respect to translation, rotation, and permutation of identical atoms, ensuring that the physical symmetries of the system are preserved.

These descriptors serve as input to a neural network, which learns the mapping between the local atomic environment and the corresponding atomic energy. This can be written as

$$E_i = f(\mathbf{D}_i), \tag{5.25}$$

where $\mathbf{D}_i$ is the descriptor vector for atom i and f represents the neural network.

In the NEP framework, this mapping is implemented using a feed-forward neural network consisting of an input layer, one or more hidden layers, and an output layer, as illustrated in Fig. 5.2. The input layer takes the descriptor vector, which contains information about distances and angles to neighboring atoms. This information is transformed through the hidden layer using nonlinear operations, allowing the model to capture complex relationships between atomic configurations and their energies. The output layer then provides the atomic energy contribution E_i. Schematic illustration of this NEP-based MLIP is shown in Figure 5.2.

During training, the parameters of the network are optimized so that the predicted energies and forces match the reference DFT values. The training process begins with a dataset of DFT-relaxed structures. Additional configurations are generated by applying small perturbations, such as random atomic displacements (rattling) and volume changes. For these configurations, single-point DFT calculations are performed to obtain energies and forces, forming the initial training dataset. The quality of the potential is then further improved using an active learning strategy. Starting from an initial model, MD simulations are performed to explore the configuration space. Configurations associated with high model uncertainty are identified and selected. These configurations are then recalculated using DFT and added to the training dataset. In addition, relaxation and high-temperature MD simulations are used to sample a broader range of configurations relevant for diffusion processes.

This procedure is repeated iteratively. At each iteration, a new model is trained on the expanded dataset, allowing the potential to progressively improve in regions of configuration space that were previously not well described. The process is continued until the errors in predicted energies and forces, as well as the model uncertainty, fall below predefined thresholds. To do this we utilized the GPUMD [77] and CALORINE packages [79]. Although this approach improves accuracy while maintaining low computational cost, the reliability of the NEP model is limited to the range of configurations included in the training dataset. For structures outside this region, the predictions may not be accurate, and careful validation is therefore required.

6

Summary of papers

Paper I

Benchmarking Halide Migration Barriers in $CsPbX_3$: Sensitivity to DFT Choices

In Paper I, we analyze halide-ion migration barriers in $CsPbX_3$ (X = I, Br, Cl) with a focus on their sensitivity to DFT methodological choices.

Reported migration barriers in HPs show a wide variation in the literature, even for similar systems and defect mechanisms. Since diffusion depends exponentially on the migration barrier, these differences lead to large variations in predicted ionic transport. It is therefore not always clear whether these differences originate from intrinsic material properties or from computational choices.

To address this issue, we perform a systematic benchmark by comparing multiple DFT setups within a consistent framework. We quantify the variation in migration barriers with respect to exchange–correlation functional, migration pathway, and defect charge state. Inter-functional tests allow us to separate structural effects from energetic contributions, showing that a large part of the variation originates from differences in relaxed lattice volume and the resulting transition-state geometry. Trends across the halide series (Cl, Br, I) are also established.

We compute migration barriers using NEB calculations for both the vacancy- and interstitial-mediated mechanisms, considering several exchange–correlation functionals, including PBE, vdW-DF-cx, r^{2}SCAN+rVV10, and PBE0.

Paper II

Vacancy migration in mixed halide perovskites

In Paper II, we develop NEP models for mixed $Cs_{1-x}Rb_xPbBr_{3(1-y)}I_{3y}$ perovskites containing halide vacancies and use them to analyze vacancy-mediated ion transport across composition, phase, and temperature.

The models are trained on DFT data using the vdW-DF-cx functional for charge neutral configuration and are applied in MD simulations over a broad compositional range. These simulations are used to evaluate vacancy migration in mixed systems by calculating ion diffusion, to examine the dependence on crystal phase and defect concentration, and to extract migration barriers from finite-temperature dynamics.

The results show that diffusivity of iodide vacancies are higher than bromide vacancies. Diffusivity also depends strongly on crystal phase, with lower barriers typically being in the cubic and tetragonal phases than in the orthorhombic phase. In addition, the halide diffusivity is not consistently increasing with composition. It show a highest in diffusion near 75% Br content. Results at different vacancy concentrations (0.1%, 0.5% and 1% vacancies), furthermore show that normalized diffusivity remains constant with vacancy concentration, with little influence from nearby defects, indicating weak correlation effects.

Paper III

Atomic-level dynamics of ion migration in metal halide perovskites

In Paper III, carried out in collaboration with experimentalists, we combine variable-temperature magic angle spinning nuclear magnetic resonance measurements with MD simulations using an MLIP to investigate atomic motion in mixed HPs under experimentally relevant conditions.

The experiments probe thermally activated atomic motion in the bulk phase, while the simulations provide atomistic access to the underlying diffusion processes and local lattice dynamics. The combined analysis is used to separate ionic diffusion from other temperature-dependent effects, in particular soft-phonon behavior, and to identify the structural origin of the observed transport trends.

The results show that compositional mixing on both the halide and A-site sub-lattices enhances the diffusivity of halide ions and A-site cations. The simulations further show that this enhanced transport originates from static local distortions introduced by ion mixing, which modify the local structural environment and facilitate atomic motion. In this way, the simulations provide an atomistic interpretation of the experimental observations and clarify how compositional disorder influences ion diffusion in HPs.

7

Conclusion and outlook

In this thesis, ion transport in inorganic HPs has been studied across different length and time scales, with the aim of understanding how defect-mediated ion migration at the atomic scale connects to diffusion at finite temperature. This combines DFT, MLIP, MD simulations, and experimental comparison to provide a consistent picture of ionic transport in these materials.

In Paper I, defect-mediated ion migration in $CsPbX_3$ was analyzed using DFT and NEB calculations. The results show that migration barriers are sensitive to computational choices, including the exchange–correlation functional, defect charge state, migration pathway, and spin–orbit coupling. In particular, the relaxed lattice structure, volume, and local bonding environment play a key role in determining the migration barrier. These results show that migration barriers reported in the literature cannot be directly compared unless the computational setup is treated consistently.

In Paper II, the focus shifts from individual migration events to ion diffusion in mixed compositions $Cs_{1-x}Rb_xPbBr_{3(1-y)}I_{3y}$. Using MD simulations based on NEP-MLIPs, diffusion coefficients are obtained over a range of temperatures and composition and analyzed using the Arrhenius relation. The results show that diffusion is governed by both activation energy and prefactor, and that compositional changes influence both contributions. In particular, halide and A-site mixing modify the lattice structure and lattice dynamics, leading to changes in ion diffusivity.

In Paper III, carried out in collaboration with experimentalists, the simulation results are linked to experimentally relevant behavior through comparison with variable-temperature MAS NMR measurements. The combined experimental–simulation analysis shows that compositional mixing enhances ionic diffusivity in the bulk phase. This increase is linked to static disorder introduced by mixing, which modifies the local structural environment and facilitates ion motion. The analysis also allows separation of diffusion-related motion from phonon-driven lattice dynamics, providing a clearer

picture of atomic motion in mixed systems.

Overall, this thesis shows that ion transport in HPs is governed by a combination of structural, chemical, and dynamical factors. Migration barriers alone are not sufficient to describe transport, as diffusion also depends on defect concentrations, lattice flexibility, and vibrational dynamics. By combining DFT-based analysis with large-scale MD and experimental comparison, this work provides a consistent framework for connecting atomistic migration mechanisms with macroscopic diffusion behavior.

Looking ahead, several directions can extend this work. While this thesis mainly focuses on vacancy-mediated ion migration, the role of interstitial defects remains less explored. In addition, A-site defect-mediated transport may become relevant in mixed systems and requires further investigation. Extending the analysis to grain boundaries, surfaces, and interfaces could also be relevant, as these features can strongly influence ion transport in real materials. Finally, moving beyond lead-based systems toward non-toxic alternatives, such as Ge-based perovskites, provides an opportunity to study how B-site chemistry and off-centering behavior influence phase stability and ion diffusion. Extending the present approach to these systems will be important for developing a more complete understanding of ion transport in HPs.

Acknowledgments

I would first like to thank my supervisor, Julia Wiktor, for her continuous support, guidance, and patience throughout this work. I am also grateful to my examiner, Paul Erhart, for his motivation and for providing valuable insights that helped deepen my understanding of the topic. I would also like to thank my co-supervisor, Richard Matthias Geilhufe, for his support. I would like to sincerely thank Erik Fransson for his inspiration, helpful discussions, encouragement, and constant support over the past year. I am also thankful to my group members for making the working environment both productive and enjoyable. A special thanks to Sangita for helping me settle into a new country and environment—your support, both big and small, has meant a lot. Thanks to my friends in Gothenburg who make my life lovely and enjoyable here. Finally, I would like to thank my family for their constant support throughout my life.

Bibliography

[1] A. Kojima, K. Teshima, Y. Shirai, and T. Miyasaka, *Organometal halide perovskites as visible-light sensitizers for photovoltaic cells,* Journal of the American Chemical Society **131**, 6050 (2009).

[2] National Renewable Energy Laboratory (NREL), *Best Research-Cell Efficiency Chart,* `https://www.nrel.gov/pv/cell-efficiency.html`, 2026. Accessed: 2026-04-14. Single-junction perovskite: 27.3%; Tandem: 34.85%.

[3] T. M. Brenner, D. A. Egger, L. Kronik, G. Hodes, and D. Cahen, *Hybrid organic—inorganic perovskites: low-cost semiconductors with intriguing charge-transport properties,* Nature Reviews Materials **1**, 1 (2016).

[4] S. D. Stranks, G. E. Eperon, G. Grancini, C. Menelaou, M. J. Alcocer, T. Leijtens, L. M. Herz, A. Petrozza, and H. J. Snaith, *Electron-hole diffusion lengths exceeding 1 micrometer in an organometal trihalide perovskite absorber,* Science **342**, 341 (2013).

[5] L. Protesescu, S. Yakunin, M. I. Bodnarchuk, F. Krieg, R. Caputo, C. H. Hendon, R. X. Yang, A. Walsh, and M. V. Kovalenko, *Nanocrystals of cesium lead halide perovskites ($CsPbX_3$, X = Cl, Br, and I): novel optoelectronic materials showing bright emission with wide color gamut,* Nano Letters **15**, 3692 (2015).

[6] Y. Zhou and Y. Zhao, *Chemical stability and instability of inorganic halide perovskites,* Energy & Environmental Science **12**, 1495 (2019).

[7] O. Yaffe, Y. Guo, L. Z. Tan, D. A. Egger, T. Hull, C. C. Stoumpos, F. Zheng, T. F. Heinz, L. Kronik, M. G. Kanatzidis, J. S. Owen, A. M. Rappe, M. A. Pimenta, and L. E. Brus, *Local Polar Fluctuations in Lead Halide Perovskite Crystals,* Phys. Rev. Lett. **118**, 136001 (2017). `doi:10.1103/PhysRevLett.118.136001`.

[8] W. Chu, Q. Zheng, O. V. Prezhdo, J. Zhao, and W. A. Saidi, *Low-frequency lattice phonons in halide perovskites explain high defect tolerance toward electron-hole recombination,* Science Advances **6**, eaaw7453 (2020).

[9] H. Zai, Y. Ma, Q. Chen, and H. Zhou, *Ion migration in halide perovskite solar cells: Mechanism, characterization, impact and suppression,* Journal of Energy Chemistry **63**, 528 (2021).

[10] K. Sakhatskyi, R. A. John, A. Guerrero, S. Tsarev, S. Sabisch, T. Das, G. J. Matt, S. Yakunin, I. Cherniukh, M. Kotyrba, *et al.*, *Assessing the drawbacks and benefits of ion migration in lead halide perovskites,* ACS Energy Letters **7**, 3401 (2022).

[11] K. Domanski, B. Roose, T. Matsui, M. Saliba, S.-H. Turren-Cruz, J.-P. Correa-Baena, C. R. Carmona, G. Richardson, J. M. Foster, F. De Angelis, *et al.*, *Migration of cations induces*

reversible performance losses over day/night cycling in perovskite solar cells, Energy & Environmental Science **10**, 604 (2017).

[12] H. Zhang, X. Fu, Y. Tang, H. Wang, C. Zhang, W. W. Yu, X. Wang, Y. Zhang, and M. Xiao, *Phase segregation due to ion migration in all-inorganic mixed-halide perovskite nanocrystals,* Nature Communications **10**, 1088 (2019).

[13] J. Thiesbrummel, J. V. Milić, C. Deibel, E. C. Garnett, S. Tao, T. Kirchartz, A. Guerrero, P. Cameron, W. Tress, M. S. Islam, and B. Ehrler, *Ion migration in perovskite solar cells,* Nature Reviews Chemistry **10**, 179 (2026). doi:10.1038/s41570-025-00790-8.

[14] C. Eames, J. M. Frost, P. R. Barnes, B. C. O'regan, A. Walsh, and M. S. Islam, *Ionic transport in hybrid lead iodide perovskite solar cells,* Nature Communications **6**, 7497 (2015).

[15] M. H. Rahman, M. Biswas, and A. Mannodi-Kanakkithodi, *Understanding defect-mediated ion migration in semiconductors using atomistic simulations and machine learning,* ACS Materials Au **4**, 557 (2024).

[16] A. Walsh, D. O. Scanlon, S. Chen, X. Gong, and S.-H. Wei, *Self-regulation mechanism for charged point defects in hybrid halide perovskites,* Angewandte Chemie International Edition **54**, 1791 (2015).

[17] J. Kang and L.-W. Wang, *High defect tolerance in lead halide perovskite $CsPbBr_3$,* The Journal of Physical Chemistry Letters **8**, 489 (2017).

[18] M. Pols, V. Brouwers, S. Calero, and S. Tao, *How fast do defects migrate in halide perovskites: insights from on-the-fly machine-learned force fields,* Chemical Communications **59**, 4660 (2023).

[19] G. Henkelman, B. P. Uberuaga, and H. Jónsson, *A climbing image nudged elastic band method for finding saddle points and minimum energy paths,* The Journal of Chemical Physics **113**, 9901 (2000).

[20] V. Tyagi, M. Pols, G. Brocks, and S. Tao, *Tracing Ion Migration in Halide Perovskites with Machine Learned Force Fields,* The Journal of Physical Chemistry Letters **16**, 5153 (2025).

[21] L. McGovern, G. Grimaldi, M. H. Futscher, E. M. Hutter, L. A. Muscarella, M. C. Schmidt, and B. Ehrler, *Reduced barrier for ion migration in mixed-halide perovskites,* ACS Applied Energy Materials **4**, 13431 (2021).

[22] K. Dey, D. Ghosh, M. Pilot, S. R. Pering, B. Roose, P. Deswal, S. P. Senanayak, P. J. Cameron, M. S. Islam, and S. D. Stranks, *Substitution of lead with tin suppresses ionic transport in halide perovskite optoelectronics,* Energy & Environmental Science **17**, 760 (2024).

[23] C. K. Møller, *Crystal structure and photoconductivity of caesium plumbohalides,* Nature **182**, 1436 (1958).

[24] A. N. Arber, Vikram, F. C. Mocanu, and M. S. Islam, *Ion Migration and Dopant Effects in the Gamma-$CsPbI_3$ Perovskite Photovoltaic Material: Atomistic Insights through Ab Initio and Machine Learning Methods,* Chemistry of Materials , (2025).

[25] G. E. Eperon, G. M. Paternò, R. J. Sutton, A. Zampetti, A. A. Haghighirad, F. Cacialli, and H. J. Snaith, *Inorganic caesium lead iodide perovskite solar cells,* Journal of Materials Chemistry A **3**, 19688 (2015).

[26] K. Wang, Z. Jin, L. Liang, H. Bian, D. Bai, H. Wang, J. Zhang, Q. Wang, and S. Liu, *All-inorganic cesium lead iodide perovskite solar cells with stabilized efficiency beyond 15%,* Nature Communications **9**, 4544 (2018).

[27] C. Ming, H. Wang, D. West, S. Zhang, and Y.-Y. Sun, *Defect tolerance in $CsPbI_3$: reconstruction of the potential energy landscape and band degeneracy in spin–orbit coupling,* Journal of Materials Chemistry A **10**, 3018 (2022).

[28] G.-W. Kim and A. Petrozza, *Defect Tolerance and Intolerance in Metal-Halide Perovskites,* Advanced Energy Materials **10**, 2001959 (2020). doi:https://doi.org/10.1002/aenm.202001959.

[29] L. Zhang, L. Mei, K. Wang, Y. Lv, S. Zhang, Y. Lian, X. Liu, Z. Ma, G. Xiao, Q. Liu, *et al.*, *Advances in the application of perovskite materials,* Nano-Micro Letters **15**, 177 (2023).

[30] X. Jia, C. Zuo, S. Tao, K. Sun, Y. Zhao, S. Yang, M. Cheng, M. Wang, Y. Yuan, J. Yang, *et al.*, *$CsPb(I_xBr_{1-x})_3$ solar cells,* Science Bulletin **64**, 1532 (2019).

[31] S. Tao, L. Polavarapu, and P. Vivo, *Perovskite photovoltaics: stability and scalability,* Scientific Reports **13**, 4370 (2023).

[32] Z. Yao, W. Zhao, and S. F. Liu, *Stability of the $CsPbI_3$ perovskite: from fundamentals to improvements,* Journal of Materials Chemistry A **9**, 11124 (2021).

[33] B. Wang and A. Navrotsky, *Thermodynamics of cesium lead halide ($CsPbX_3$, X = I, Br, Cl) perovskites,* Thermochimica Acta **695**, 178813 (2021).

[34] D. S. Tsvetkov, M. O. Mazurin, V. V. Sereda, I. L. Ivanov, D. A. Malyshkin, and A. Y. Zuev, *Formation thermodynamics, stability, and decomposition pathways of $CsPbX_3$ (X = Cl, Br, I) photovoltaic materials,* The Journal of Physical Chemistry C **124**, 4252 (2020).

[35] Y. Xiang, H. Xin, C. Wang, F. Zhou, H. Zhang, P. Hang, L. Xu, X. Yu, J. Xue, D. Yang, *et al.*, *Mechanistic insights into defect-governed ion migration and phase instability in mixed-halide perovskites,* Journal of Materials Chemistry A , (2026).

[36] S.-W. Lee, S. Kim, S. Bae, K. Cho, T. Chung, L. E. Mundt, S. Lee, S. Park, H. Park, M. C. Schubert, *et al.*, *UV degradation and recovery of perovskite solar cells,* Scientific Reports **6**, 38150 (2016).

[37] D. Bryant, N. Aristidou, S. Pont, I. Sanchez-Molina, T. Chotchunangatchaval, S. Wheeler, J. R. Durrant, and S. A. Haque, *Light and oxygen induced degradation limits the operational stability of methylammonium lead triiodide perovskite solar cells,* Energy & Environmental Science **9**, 1655 (2016).

[38] J. Wang, G. Jin, Q. Zhen, C. He, and Y. Duan, *Bulk passivation and interfacial passivation for perovskite solar cells: which one is more effective?,* Advanced Materials Interfaces **8**, 2002078 (2021).

[39] A. Walsh and S. D. Stranks, *Taking control of ion transport in halide perovskite solar cells,* ACS Energy Letters **3**, 1983 (2018).

[40] B.-w. Park and S. I. Seok, *Intrinsic instability of inorganic–organic hybrid halide perovskite materials,* Advanced Materials **31**, 1805337 (2019).

[41] E. Fransson, J. Wiktor, and P. Erhart, *Phase Transitions in Inorganic Halide Perovskites from Machine-Learned Potentials,* The Journal of Physical Chemistry C **127**, 13773 (2023). doi:10.1021/acs.jpcc.3c01542.

[42] J. Li, F. Pan, G.-X. Zhang, Z. Liu, H. Dong, D. Wang, Z. Jiang, W. Ren, Z.-G. Ye, M. Todorović, *et al.*, *Structural disorder by octahedral tilting in inorganic halide perovskites: New insight with Bayesian optimization,* Small Structures **5**, 2400268 (2024).

[43] J. Klarbring, *Low-energy paths for octahedral tilting in inorganic halide perovskites,* Physical Review B **99**, 104105 (2019).

[44] R. X. Yang, J. M. Skelton, E. L. Da Silva, J. M. Frost, and A. Walsh, *Spontaneous octahedral tilting in the cubic inorganic cesium halide perovskites $CsSnX_3$ and $CsPbX_3$ (X = F, Cl, Br, I),* The Journal of Physical Chemistry Letters **8**, 4720 (2017).

[45] S. Kar and K. Dey, *Instabilities and Degradation in Perovskite Materials and Devices,* in *Perovskite Optoelectronic Devices* (Springer, 2024), p. 573.

[46] J. Zhang, X. Zhang, M. E. Turiansky, and C. G. Van de Walle, *Iodine vacancies do not cause nonradiative recombination in halide perovskites,* PRX Energy **2**, 013008 (2023).

[47] D. Meggiolaro, S. G. Motti, E. Mosconi, A. J. Barker, J. Ball, C. A. R. Perini, F. Deschler, A. Petrozza, and F. De Angelis, *Iodine chemistry determines the defect tolerance of lead-halide perovskites,* Energy & Environmental Science **11**, 702 (2018).

[48] G. Sarkar, P. Deswal, and D. Ghosh, *Ion diffusion dynamics and halogen mixing at the heterojunction of halide perovskites: atomistic insights,* The Journal of Physical Chemistry C **128**, 1762 (2024).

[49] J. Wiktor, E. Fransson, D. Kubicki, and P. Erhart, *Quantifying Dynamic Tilting in Halide Perovskites: Chemical Trends and Local Correlations,* Chemistry of Materials **35**, 6737 (2023). doi:10.1021/acs.chemmater.3c00933.

[50] J. M. Azpiroz, E. Mosconi, J. Bisquert, and F. De Angelis, *Defect migration in methylammonium lead iodide and its role in perovskite solar cell operation,* Energy & Environmental Science **8**, 2118 (2015).

[51] R.-I. Biega and L. Leppert, *Halogen vacancy migration at surfaces of $CsPbBr_3$ perovskites: insights from density functional theory,* Journal of Physics: Energy **3**, 034017 (2021).

[52] K. Miskin, Y. Cao, M. Marland, F. Shaikh, D. T. Moore, J. A. Marohn, and P. Clancy, *Low-energy pathways lead to self-healing defects in $CsPbBr_3$,* Physical Chemistry Chemical Physics **27**, 15446 (2025).

[53] M. R. Samatov, D. Liu, L. Zhao, E. A. Kazakova, D. A. Abrameshin, A. Das, A. S. Vasenko, and O. V. Prezhdo, *Ion Migration at Metal Halide Perovskite Grain Boundaries Elucidated with a Machine Learning Force Field,* The Journal of Physical Chemistry Letters **15**, 12362 (2024).

[54] G. Zhang, J. Zhang, Z. Yang, Z. Pan, H. Rao, and X. Zhong, *Role of Moisture and Oxygen in Defect Management and Orderly Oxidation Boosting Carbon-Based $CsPbI_2Br$ Solar Cells to a New Record Efficiency,* Advanced Materials **34**, 2206222 (2022).

[55] L. Cao, Y. Tong, H. Wang, and K. Wang, *Challenges and modification strategies of air-processed all-inorganic $CsPbX_3$ perovskite films for efficient photovoltaics,* Energy Materials **4**, N (2024).

[56] T. Hussain, K. Fatima, A. Anjum, T. A. Abbas, I. Ahmad, A. Fakharuddin, and M. Sultan, *Experimental evidence of ion migration in aged inorganic perovskite solar cells using non-destructive RBS depth profiling,* Materials Advances **3**, 7846 (2022).

[57] Y. W. Woo, Y.-K. Jung, G. Y. Kim, S. Kim, and A. Walsh, *Factors influencing halide vacancy transport in perovskite solar cells,* Discover Materials **2**, 8 (2022).

[58] T. J. Smolders, A. B. Walker, and M. J. Wolf, *3D-to-2D transition of anion vacancy mobility in $CsPbBr_3$ under hydrostatic pressure,* The Journal of Physical Chemistry Letters **12**, 5169 (2021).

[59] F. P. Sabino, X. G. Zhao, G. M. Dalpian, and A. Zunger, *Impact of symmetry breaking and spin-orbit coupling on the band gap of halide perovskites,* Physical Review B **110**, 035160 (2024).

[60] C. Vona, D. Nabok, and C. Draxl, *Electronic Structure of (Organic-) Inorganic Metal Halide Perovskites: The Dilemma of Choosing the Right Functional,* Advanced Theory and Simulations **5**, 2100496 (2022).

[61] A. V. Cohen, D. A. Egger, A. M. Rappe, and L. Kronik, *Breakdown of the static picture of defect energetics in halide perovskites: the case of the Br vacancy in $CsPbBr_3$,* The Journal of Physical Chemistry Letters **10**, 4490 (2019).

[62] D. Frenkel and B. Smit, *Understanding molecular simulation: from algorithms to applications* (elsevier, 2023).

[63] V. Tyagi, M. Pols, G. Brocks, and S. Tao, *Halide diffusion in mixed-halide perovskites and heterojunctions,* arXiv preprint arXiv:2601.11503 , (2026).

[64] W. J. Baldwin, X. Liang, J. Klarbring, M. Dubajic, D. Dell'Angelo, C. Sutton, C. Caddeo, S. D. Stranks, A. Mattoni, A. Walsh, and G. Csányi, *Dynamic Local Structure in Caesium Lead Iodide: Spatial Correlation and Transient Domains,* Small , 2303565 (2023). doi:10.1002/smll.202303565.

[65] Y. Zhong, J. Yang, X. Wang, Y. Liu, Q. Cai, L. Tan, and Y. Chen, *Inhibition of ion migration for highly efficient and stable perovskite solar cells,* Advanced Materials **35**, 2302552 (2023).

[66] H. Eschrig, *The fundamentals of density functional theory* (Springer, 1996).

[67] J. P. Perdew, E. R. McMullen, and A. Zunger, *Density-functional theory of the correlation energy in atoms and ions: a simple analytic model and a challenge,* Physical Review A **23**, 2785 (1981).

[68] P. Ziesche, S. Kurth, and J. P. Perdew, *Density functionals from LDA to GGA,* Computational Materials Science **11**, 122 (1998).

[69] J. P. Perdew, M. Ernzerhof, and K. Burke, *Rationale for mixing exact exchange with density functional approximations,* The Journal of chemical physics **105**, 9982 (1996).

[70] J. W. Furness, A. D. Kaplan, J. Ning, J. P. Perdew, and J. Sun, *Accurate and numerically efficient r2SCAN meta-generalized gradient approximation,* The journal of Physical Chemistry Letters **11**, 8208 (2020).

[71] J. Ning, M. Kothakonda, J. W. Furness, A. D. Kaplan, S. Ehlert, J. G. Brandenburg, J. P. Perdew, and J. Sun, *Workhorse minimally empirical dispersion-corrected density functional with tests for weakly bound systems: r2SCAN+rVV10,* Physical Review B **106**, 075422 (2022).

[72] R. Sabatini, T. Gorni, and S. De Gironcoli, *Nonlocal van der Waals density functional made simple and efficient,* Physical Review B—Condensed Matter and Materials Physics **87**, 041108 (2013).

[73] K. Berland, C. A. Arter, V. R. Cooper, K. Lee, B. I. Lundqvist, E. Schröder, T. Thonhauser, and P. Hyldgaard, *van der Waals density functionals built upon the electron-gas tradition: Facing the challenge of competing interactions,* The Journal of chemical physics **140**, (2014).

[74] B. Xu, J. Zhang, Y. Xiong, S. Ma, Y. Osetsky, and S. Zhao, *Mechanism of sluggish diffusion under rough energy landscape,* Cell Reports Physical Science **4**, (2023).

[75] L. Verlet, *Computer" experiments" on classical fluids. I. Thermodynamical properties of Lennard-Jones molecules,* Physical Review **159**, 98 (1967).

[76] J. R. Ray and H. Zhang, *Correct microcanonical ensemble in molecular dynamics,* Physical Review E **59**, 4781 (1999).

[77] Z. Fan, Y. Wang, P. Ying, K. Song, J. Wang, Y. Wang, Z. Zeng, K. Xu, E. Lindgren, J. M. Rahm, A. J. Gabourie, J. Liu, H. Dong, J. Wu, Y. Chen, Z. Zhong, J. Sun, P. Erhart, Y. Su, and T. Ala-Nissila, *GPUMD: A package for constructing accurate machine-learned potentials and performing highly efficient atomistic simulations,* The Journal of Chemical Physics **157**, 114801 (2022). doi:10.1063/5.0106617.

[78] K. Song, R. Zhao, J. Liu, Y. Wang, E. Lindgren, Y. Wang, S. Chen, K. Xu, T. Liang, P. Ying, N. Xu, Z. Zhao, J. Shi, J. Wang, S. Lyu, Z. Zeng, S. Liang, H. Dong, L. Sun, Y. Chen, Z. Zhang, W. Guo, P. Qian, J. Sun, P. Erhart, T. Ala-Nissila, Y. Su, and Z. Fan, *General-purpose machine-learned potential for 16 elemental metals and their alloys,* Nature Communications **15**, 10208 (2024). doi:10.1038/s41467-024-54554-x.

[79] E. Lindgren, M. Rahm, E. Fransson, F. Eriksson, N. Österbacka, Z. Fan, and P. Erhart, *calorine: A Python package for constructing and sampling neuroevolution potential models,* Journal of Open Source Software **9**, 6264 (2024). doi:10.21105/joss.06264.